Biosensors and Bioelectronics 127 (2019) 64–71

Contents lists available at ScienceDirect

Biosensors and Bioelectronics

journal homepage: www.elsevier.com/locate/bios

High-activity Fe_3O_4 nanozyme as signal amplifier: A simple, low-cost but efficient strategy for ultrasensitive photoelectrochemical immunoassay

Wenshi Li, Gao-Chao Fan*, Fengxian Gao, Yige Cui, Wei Wang, Xiliang Luo*

Key Laboratory of Optic-electric Sensing and Analytical Chemistry for Life Science, MOE; Shandong Key Laboratory of Biochemical Analysis; Key Laboratory of Analytical Chemistry for Life Science in Universities of Shandong; College of Chemistry and Molecular Engineering, Qingdao University of Science and Technology, Qingdao 266042, PR China

ARTICLE INFO

Keywords:
Photoelectrochemistry
Nanozyme
Immunoassay
Signal amplifier
Fe_3O_4

ABSTRACT

Sensitive but with simple, inexpensive detection of disease-related biomarkers in real biological samples is of quite necessity for early diagnosis and disease surveillance. We herein first introduced high-activity Fe_3O_4 nanozyme as signal amplifier to develop an ultrasensitive photoelectrochemical (PEC) immunoassay, which meanwhile has the distinct merits of both simplicity and low cost compared with previously reported enzyme-labeling PEC immunoassays. In the proposal, to illustrate and describe the PEC platform, prostate-specific antigen (PSA, Ag) was used as a target model. Specifically, ZnO nanorods (ZnO-NRs) grown vertically on a bare indium–tin oxide (ITO) electrode was deposited with $ZnIn_2S_4$ nanocrystals, producing $ZnIn_2S_4$/ZnO-NRs/ITO photoelectrode as the PEC matrix to modify capture PSA antibody (Ab_1). Histidine-modified Fe_3O_4 (his-Fe_3O_4) nanozyme as signal amplifier was linked with signal PSA antibody (Ab_2) to form his-Fe_3O_4@Ab_2 conjugate, and was anchored through specific sandwich immunoreaction. The labeling his-Fe_3O_4 nanozyme acted as a peroxidase to induce the generation of the insoluble and insulating precipitation, resulting in an evident decrease in the photocurrent signal. On account of combined effects of high catalytic efficiency of the his-Fe_3O_4 nanozyme and excellent PEC properties of the $ZnIn_2S_4$/ZnO-NRs/ITO photoelectrode, ultralow detection limit of 18 fg/mL for target Ag detection was achieved. Besides, as high-activity his-Fe_3O_4 nanozyme has substituted natural enzyme as signal amplifier, simplicity and low cost of the PEC immunoassay was realized.

1. Introduction

Highly sensitive, precise and inexpensive detection of disease-associated biomarkers shows great promise for early diagnosis, prognosis, and timely treatment of the important diseases or cancers (Ludwig and Weinstein, 2005; Weston and Hood, 2004; Sahab et al., 2007). Photoelectrochemical (PEC) immunoassay as a powerful and promising technique for biomarkers detection has gained extensive attention (Zhao et al., 2018). Owning to the salient features of simple, portable, inexpensive and easy-operated instrument, it is well qualified for rapid and high-throughput analysis (Haddour et al., 2006; Wang et al., 2009a). Besides, PEC immunoassay also has a low background signal due to different energy forms of the input and output signals, benefiting the promotion of the sensitivity (Liang et al., 2006; Wang et al., 2009b). Of course, PEC properties (mainly including photocurrent output and stability) of the photoactive species plays a vital role in performances of the PEC immunoassay. To date, semiconductor nanomaterials are the most widely used to fabricate the PEC immunosensors. Thereinto, cadmium-based species such as CdS, CdSe, CdTe and their derivatives are usually included because of the higher photocurrent output (Fan et al., 2014, 2017a, 2016; Zhao et al., 2014; Wang et al., 2015; Lin et al., 2016). But for the purpose of practical use, the PEC immunoassay developed on non-toxic or low-toxicity photoactive nanomaterials with excellent properties is just desirable.

To pursue high sensitivity, various signal amplifiers have been reported in the labeling PEC immunoassays, such as horse radish peroxidase (HRP) (Zhao et al., 2012b; Ge et al., 2016), glucose oxidase (GOx) (Li et al., 2012; Shu et al., 2016), alkaline phosphatase (ALP) (Zhao et al., 2012a; Cao et al., 2018), SiO_2 nanoparticle (Fan et al., 2014), polystyrene sphere (Fan et al., 2017a), CuS nanocrystal (Fan et al., 2016; Dong et al., 2018), etc. Among them, natural enzymes are very popular and often used as labels conjugated with signal antibodies to evidently amplify the photocurrent signal. Yet, the utilization of natural enzymes (such as HRP, GOx and ALP) obviously increased the expenditure of the sensor fabrication, and meanwhile the storage needs harsh conditions to keep enzyme activity. To overcome the

* Corresponding authors.
E-mail addresses: gcfan@qust.edu.cn (G.-C. Fan), xiliangluo@qust.edu.cn (X. Luo).

https://doi.org/10.1016/j.bios.2018.11.043
Received 29 August 2018; Received in revised form 6 November 2018; Accepted 27 November 2018
Available online 07 December 2018
0956-5663/

shortcomings of natural enzymes, nanozymes (which means the nanomaterials exhibiting enzyme-like properties) have attracted intense interest (Singh et al., 2017; Wei and Wang, 2013; Gao et al., 2017). Various nanomaterials have been studied to mimic the activities of peroxidase (Zhang et al., 2017), catalase (Mu et al., 2014), oxidase (Asati et al., 2009), superoxide dismutase (Mu et al., 2016), etc. Thereinto, peroxidase mimics, especially ferromagnetic (Fe_3O_4) nanoparticle, are the most popular, which have shown the promising applications in the area of biological analysis. Compared with nature enzyme HRP, Fe_3O_4 nanozyme has the distinct merits of simple preparation, easy production, lower cost of synthesis, higher stability in harsh conditions, and flexible storage conditions (Wei and Wang, 2008; Wu et al., 2018a; Wang et al., 2017a, 2017b; Tian et al., 2018). Thus, using Fe_3O_4 nanozyme instead of nature enzyme HRP as signal amplifier would make the PEC immunoassay simple and inexpensive. Besides, the activity of Fe_3O_4 nanozyme is a key point to influence the sensitivity of the PEC immunoassay, thus high activity of the synthesized Fe_3O_4 nanozyme is necessary. To best of our knowledge, however, the concept and utilization of "nanozyme" has not appeared in the PEC immunoassay.

Inspired by the research basics above, we herein developed a simple, low-cost PEC immunoassay for ultrasensitive detection of target biomarker by adopting high-activity Fe_3O_4 nanozyme as the signal amplifier and utilizing $ZnIn_2S_4$/ZnO-NRs/ITO photoelectrode as the PEC matrix, as illustrated in Scheme 1. Prostate-specific antigen (PSA, Ag) was used as a target model, rising levels of which was associated with prostate cancer. Firstly, ZnO-NRs were grown vertically on a bare ITO electrode, and $ZnIn_2S_4$ nanocrystals were then deposited on, which as a result produced the $ZnIn_2S_4$/ZnO-NRs/ITO photoelectrode. Subsequently, Ab_1 was modified on the photoelectrode via the connection of chitosan (CS) molecules. After blocking unbound sites of the Ab_1-modified electrode with bovine serum albumin (BSA), the immunosensor was ready for use. To detect target Ag, a certain concentration of Ag was firstly anchored on the sensor by specific immunoreaction with Ab_1, and then his-Fe_3O_4@Ab_2 conjugate as signal amplifier was further anchored via specific immunoreaction between Ag and Ab_2. After the immunosensor was finally incubated in H_2O_2 solution coexisting with 4-chloro-1-naphthol (4-CN), the PEC detection of target Ag was achieved via a remarkable decrease in the photocurrent signal which was produced by high-activity Fe_3O_4 nanozyme-induced catalytic precipitation (CP). The introduction of high-activity nanozyme as signal amplifier in PEC immunoassay offered a general consideration to explore other nanozyme-based PEC sensors with well analytical performances.

2. Experimental

2.1. Materials and reagents

ITO electrodes (type JH52, ITO coating 30 ± 5 nm, sheet resistance ≤ 10 Ω/square) were ordered from Beijinjing Zhongjingkeyi Technology Co., Ltd. (China). Zinc acetate dehydrate ($Zn(AC)_2{\cdot}2H_2O$), hexamethylenetetramine ($C_6H_{12}N_4$), sodium sulfide ($Na_2S{\cdot}9H_2O$), zinc nitrate hexahydrate ($Zn(NO_3)_2{\cdot}6H_2O$), indium chloride tetrahydrate ($InCl_3{\cdot}4H_2O$), ferric chloride hexahydrate ($FeCl_3{\cdot}6H_2O$), sodium acetate anhydrous (NaAc), and sodium citrate tribasic dehydrate ($Na_3C_6H_5O_7{\cdot}2H_2O$) were all purchased from the Alfa Aesar (China). Glutaraldehyde (GLD, 25% aqueous solution), 3,3′,5,5′-tetramethylbenzidine (TMB), and ascorbic acid (AA) were obtained from Aladdin Reagent Inc. (China). Chitosan powder (CS, from crab cells, 85% deacetylation), 1-ethyl-3-(3-dimethylaminopropyl) carbodiimide hydrochloride (EDC), N-hydroxysuccinimide (NHS), histidine, 4-chloro-1-naphthol (4-CN), horserdish peroxidase (HRP), and bovine serum albumin (BSA) were supplied by Sigma-Aldrich (USA). Hydrogen peroxide (H_2O_2), sodium hydroxide (NaOH), and ethylene glycol (EG) were purchased from Sinopharm Chemical Reagent Co., Ltd. (China). Prostate-specific antigen (PSA, Ag), capture PSA antibody (Ab_1), signal PSA antibody (Ab_2), α-fetoprotein (AFP), human IgG (HIgG),

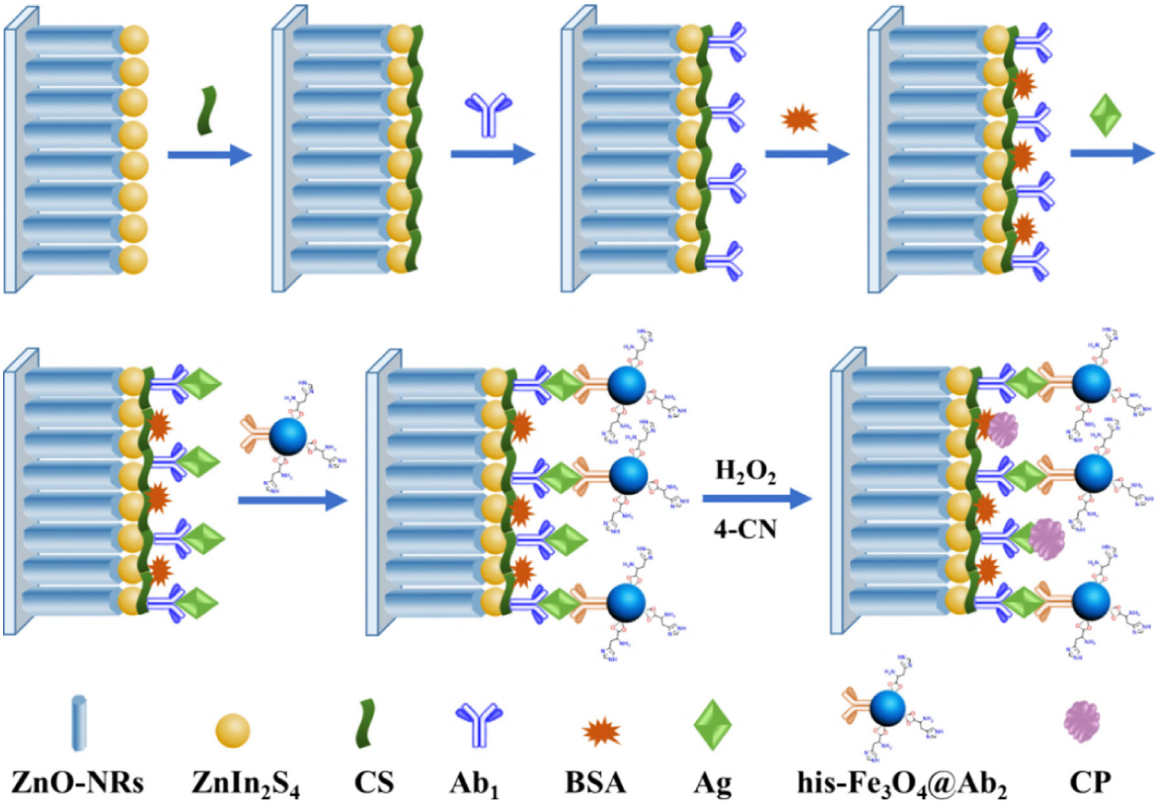

Scheme 1. Development of the PEC immunoassay using high-activity Fe_3O_4 nanozyme as signal amplifier.

carcinoembryonic antigen (CEA), and human interleukin-6 (IL-6) were obtained from Shanghai Linc-Bio Science Co. Ltd. (China). All other reagents were of analytical grade and used as received. All aqueous solutions were prepared with deionized water (DI water, 18 MΩ/cm), which was obtained from a Milli-Q water purification system. Phosphate buffer solution (PBS, pH 7.4, 10 mM) was used for the preparation of the antibody and antigen solution, washing buffer solution, and blocking buffer solution which contained 1% (w/v) BSA.

2.2. Apparatus

The microwave synthesis was performed with a XH-800S Microwave parallel synthesis system (Beijing Xianghu Science and Technology Development Co. Ltd., China). Field-emission scanning electron microscopy (FE-SEM) was carried out on a Hitachi S-4800 scanning electron microscope (Hitachi Co., Japan). Transmission electron microscopy (TEM) was performed with a JEOL-2100 transmission electron microscope (JEOL, Japan). Powder X-ray diffraction (XRD) pattern was obtained from a Philips X'pert Pro X-ray diffractometer (Cu Kα radiation, λ = 0.15418 nm, Netherlands). The UV–vis diffuse reflectance spectra were recorded on a spectrophotometer (Hitachi U-3010, Japan) with fine $BaSO_4$ powder as reference. Dynamic light scattering (DLS) characterization was performed by a ZETASIZER nanoseries (Nano-ZS, Malvern, U.K.). The UV–visible (UV–vis) absorption spectra were tested on a UV-3600 UV–visible spectrophotometer (Shimadzu, Japan). Electrochemical impedance spectroscopy (EIS) was performed on an Autolab potentiostat/galvanostat (PGSTAT 30, Eco Chemie B.V., Utrecht, Netherlands) with a three-electrode system in 0.1 M KCl solution containing 5.0 mM $K_3[Fe(CN)_6]/K_4[Fe(CN)_6]$ (1:1) mixture as a redox probe, and recorded in the frequency range of 0.01 Hz–100 kHz with an amplitude of 50 mV. Photoelectrochemical (PEC) measurements were performed with a homebuilt PEC system. A 150 W xenon lamp was utilized as the irradiation source with the light intensity of 300 mW cm^{-2} estimated by a radiometer (Photoelectric Instrument of Beijing Saifan Co., LTD., China). Photocurrent output was recorded on a CHI 760D electrochemical workstation (Shanghai Chenhua Apparatus Corporation, China) with a three-electrode system: a 0.25 cm^2 modified ITO as working electrode, a Pt wire as counter electrode, and a saturated Ag/AgCl electrode as reference electrode.

2.3. Fabrication of $ZnIn_2S_4$/ZnO-NRs/ITO photoelectrode

The ITO electrodes were first cleaned by ultrasonic treatment for 10 min in acetone, 1 M NaOH of water/ethanol mixture (1:1, v/v) and water in sequence, and then dried at 90 °C. ZnO nanorods perpendicular to an ITO electrode was prepared by an aqueous chemical method (Yu et al., 2014). Typically, the seed layer of ZnO was formed onto the substrate by dropping 5 mM $Zn(AC)_2$ ethanol solution onto a clean ITO electrode, keeping for 10 s, washing with clean ethanol, and drying with N_2 gas. This procedure was repeated 10 times, and then the electrode was annealed at 350 °C for 30 min to form the ZnO nanocrystalline layer. Subsequently, the seeded ITO electrode was immersed in an aqueous solution containing 25 mM $Zn(NO_3)_2$ and 25 mM $C_6H_{12}N_4$ at 95 °C for 3 h. The electrode was further annealed in air at 400 °C for 1 h to improve the crystallinity and decrease the interfacial defects of the as-grown ZnO nanorods.

The deposition of $ZnIn_2S_4$ nanocrystals on the ZnO-NRs/ITO electrode was according to a successive ionic layer adsorption and reaction method (Wu et al., 2018b). The ZnO-NRs/ITO electrode was immersed in a 0.1 M $Zn(NO_3)_2$ methanol solution, a 0.1 M Na_2S methanol/water mixture (1:1, v/v), a 0.1 M $InCl_3$ methanol solution, and a 0.1 M Na_2S methanol/water mixture (1:1, v/v) in sequence for 2 min of each, with intermediate methanol washing. This SILAR cycle was repeated four times. And the $ZnIn_2S_4$/ZnO-NRs/ITO photoelectrode was finally acquired after being annealed at 180 °C for 1 h in air atmosphere.

2.4. Preparation of his-Fe_3O_4@Ab_2 conjugate

Based on previous report (Fan et al., 2017b), histidine-coated Fe_3O_4 (his-Fe_3O_4) nanozyme was synthesized by a microwave-assisted solvothermal method. $FeCl_3$ (2.6 mM), NaAc (17.6 mM), and histidine (3 mM) were dispersed evenly in 40 mL of EG in order under continuous stirring at room temperature for 30 min. The solution above was then transferred into a microwave reaction kettle and reacted at 240 °C for 30 min. The resulting his-Fe_3O_4 nanozyme was rinsed with water to remove the unreacted solvent, and then dried at 50 °C several hours to obtain power products.

The preparation of his-Fe_3O_4@Ab_2 conjugate was described as below. Typically, 0.5 mL of 100 μg/mL Ab_2 solution was firstly activated by 0.5 mL of 10 mg/mL EDC/NHS at room temperature for 30 min. Then, the as-obtained his-Fe_3O_4 nanozyme was dispersed into the activated Ab_2 solution and incubated for 4 h under shaking at 4 °C. The his-Fe_3O_4@Ab_2 conjugate was purified by magnet and DI water several times, and then dispersed to 2 mL by 10 mM of PBS (pH 7.4).

2.5. Kinetic analysis of his-Fe_3O_4 nanozyme as a peroxidase

The kinetic parameters of his-Fe_3O_4 nanozyme were measured by monitoring the absorbance change at 652 nm on UV–vis spectrophotometer in time-course mode (Gao et al., 2007). The kinetic assay was carried out using his-Fe_3O_4 in 500 μL of reaction buffer (0.2 M NaAc buffer, pH 3.5) in the presence of 600 μM TMB. The kinetic analysis of Fe_3O_4 with TMB as the substrate was performed by varying the concentration of H_2O_2. After H_2O_2 was added, color reaction was found immediately. The absorbance changes at 652 nm were calculated to molar concentration changes of H_2O_2 by using a molar absorption coefficient of 39000 M^{-1} cm^{-1} for TMB-derived oxidation products according to the Beer-Lambert Law.

The Michaelis-Menten kinetic parameters were calculated by using Lineweaver-Burk plots of the double reciprocal of the function $\nu = V_{max} \times [S]/(K_M + [S])$; where ν, V_{max}, [S], and K_M represent the initial velocity, the maximal reaction velocity, the substrate concentration, and the Michaelis-Menten constant, respectively. The value of k_{cat} was calculated according to the formula of $k_{cat} = V_{max}/[E]$ (Zhang et al., 2017).

2.6. Immunoassay development

Typically, the $ZnIn_2S_4$/ZnO-NRs/ITO photoelectrode was first covered with 15 μL of 0.1 wt% CS solution in 1% acetic acid, and dried at 50 °C. After being washed with 0.1 M NaOH solution and DI water repeatedly, 20 μL of 5 wt% GLD solution was spread on the electrode and maintained at room temperature for 30 min. The electrode was then rinsed with DI water several times to remove physically adsorbed or unbound GLD. After each of the following modification step, the electrode needs to be rinsed with washing buffer solution. Specifically, 20 μL of 100 μg/mL of Ab_1 was distributed on the electrode and incubated at 4 °C for overnight. To block the nonspecific binding sites, the electrode was incubated with 20 μL of BSA blocking buffer solution at room temperature for 1 h. Subsequently, a certain concentration of PSA (target Ag) was introduced onto the electrode surface by incubating 20 μL of different concentrations of PSA at room temperature for 1 h. After the specific immunoreaction between Ab_1 and target Ag, the electrode suffered from his-Fe_3O_4 nanozyme labeling via the specific immunoreaction between target Ag and Ab_2 by additional incubation with 20 μL of his-Fe_3O_4@Ab_2 conjugate for 1 h at room temperature. Eventually, the electrode was incubated in the PBS (pH = 7.0) containing 0.2 mM H_2O_2 and 1 mM 4-CN at room temperature for 10 min before PEC detection.

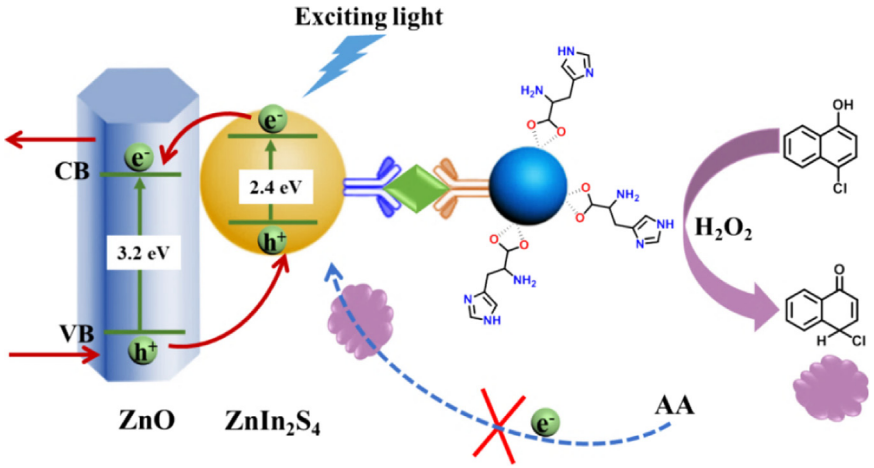

Scheme 2. Photogenerated electron-hole transfer mechanism of the PEC immunoassay for the detection of target Ag.

2.7. PEC measurement

The PEC detection was carried out in PBS (pH 7.4, 0.1 M) containing 0.1 M ascorbic acid (AA), which acted as sacrificial reagents offering electrons to PEC electrode. A xenon lamp with a spectral range of 300–2500 nm was used as irradiation source, and it was switched on and off every 10 s. The electrochemical method applied was chronoamperometry, and the external voltage was 0.0 V.

3. Results and discussion

3.1. Design principle

The photogenerated electron-hole transfer mechanism of the proposed PEC immunoassay was illustrated in Scheme 2. The $ZnIn_2S_4$/ZnO-NRs/ITO photoelectrode had excellent PEC properties of remarkable photocurrent output and high stability. ZnO is a wide-band-gap semiconductor (~ 3.2 eV), which has distinct merits of high stability, good biocompatibility and environmentally friendly (Greene et al., 2003; Zhan et al., 2013). One-dimensional (1D) semiconductor nanomaterials such as nanowires, nanorods and nanotubes have attracted extensive interests since they could evidently enlarge the specific surface area and offer direct pathway for photogenerated electron transfer, contributing to significant inhibition of the electron-hole recombination (Wang et al., 2010; Zhang et al., 2016). Thus the morphology of nanorod was adopted herein. However, ZnO can absorb only the ultraviolet light, which limits the utilization of light energy. $ZnIn_2S_4$ is one of the ternary chalcogenides with good chemical stability, and it has a smaller energy band-gap (~ 2.4 eV) (Liu et al., 2014; Han et al., 2015). Coupling $ZnIn_2S_4$ with ZnO can effectively harvest visible light, and the stepwise band-edge levels of ZnO and $ZnIn_2S_4$ benefits the injection of excited electrons from $ZnIn_2S_4$ to ZnO, which hence evidently promotes the photocurrent output (Han et al., 2015; Bai et al., 2015).

Magnetite (Fe_3O_4) is an abundant natural mineral with environmental compatibility and high surface redox activity. Since Fe_3O_4 nanozyme has been found to exhibit an intrinsic peroxidase-like activity in 2007 (Gao et al., 2007), its application in various bioanalysis areas has been widely studied. The design of histidine-modified Fe_3O_4 (his-Fe_3O_4) nanozyme was inspired by the specific configuration of active site in HRP (Veitch, 2004). Concisely, the distal imidazole of His42 helps the location of H_2O_2 molecule into the active site cavity via H-bond interaction, which plays a crucial role in holding H_2O_2 in place (Veitch, 2004). High activity of his-Fe_3O_4 nanozyme originated from enhanced affinity with H_2O_2 through H-bond formation between imidazole group of histidine and H_2O_2 (Fan et al., 2017b). After the his-Fe_3O_4@Ab_2 conjugate was bound on the immunosensor via specific immunoreaction between target Ag and Ab_2, the high-activity his-Fe_3O_4 nanozyme catalyzed H_2O_2 to oxidize 4-CN and generated insulating precipitation of benzo-4-chlorohexadienone on the sensor surface (Zhao et al., 2012b; Ge et al., 2016), causing the blocking of the electron transfer. And hereby the target Ag could be quantitatively detected by the decrement of the photocurrent signal.

3.2. Characterization of the $ZnIn_2S_4$/ZnO-NRs/ITO photoelectrode

The surface topography of the $ZnIn_2S_4$/ZnO-NRs/ITO photoelectrode was first characterized by scanning electron microscopy (SEM). As exhibited in Fig. 1A, highly ordered ZnO nanorods with hexagonal structure were vertically grown on the ITO electrode, and their diameter was about 70–100 nm. After $ZnIn_2S_4$ nanocrystals deposition, as shown in Fig. 1B, plenty of small-sized nanoparticles were found to adhere on the ZnO nanorods and the electrode surface becomes very rough, illustrating successful modification of the $ZnIn_2S_4$ nanocrystals. To verify the formation of $ZnIn_2S_4$/ZnO-NRs structure, transmission electron microscopy (TEM) was performed. As shown in Fig. S1, the surface of a randomly-selected nanorod was covered with plenty of nanoparticles. It could be observed from high-resolution TEM image in the inset of Fig. S1 that the sample was made up of different crystal phases, in which the fringe spacings of 0.26 nm and 0.29 nm matched well with the interplanar spacings of the (002) plane of wurtzite type ZnO and (104) plane of $ZnIn_2S_4$, respectively. X-ray diffraction (XRD) was further used to characterize the $ZnIn_2S_4$/ZnO-NRs/ITO photoelectrode. As shown in Fig. 1C, the blue curve is the typical XRD pattern of the ZnO-NRs on an ITO substrate. All of the characteristic diffraction peaks located at 2θ = 31.7°, 34.52°, 36.68°, 47.5°, 56.56°, 62.82° and 67.92° could be assigned to (100), (002), (101), (102), (110), (103) and (200) of hexagonal phase ZnO (JCPDS card no. 65-3411). The ultrahigh spike at 34.52° toward ZnO (002) plane indicates the ZnO-NRs are highly c-axis oriented (Wang et al., 2008), which was consistent with the hexagonal faces seen in the SEM of Fig. 1A. After $ZnIn_2S_4$ deposition (red curve), additional diffraction peaks at 21.5°, 27.6°, 30.4°, 39.7°, 47.7°, 52.2° and 56.2° could be indexed to planes (006), (102), (104), (108), (112), (1012) and (203) of hexagonal $ZnIn_2S_4$ (JCPDS card no.72–0773). No impurity peaks were detected, indicating formation of the pure products. Fig. 1D exhibits UV–vis diffuse reflection spectra of the ZnO-NRs/ITO and $ZnIn_2S_4$/ZnO-NRs/ITO electrodes. The absorption edge of the pure ZnO-NRs was located at about 405 nm with the band-gap value of 3.06 eV. After $ZnIn_2S_4$ deposition, the $ZnIn_2S_4$/ZnO-NRs/ITO electrode had an absorption edge at about 480 nm, corresponding to the band-gap value of 2.58 eV. As a result, the light harvest of the $ZnIn_2S_4$/ZnO-NRs/ITO electrode is greatly enhanced in visible-light region.

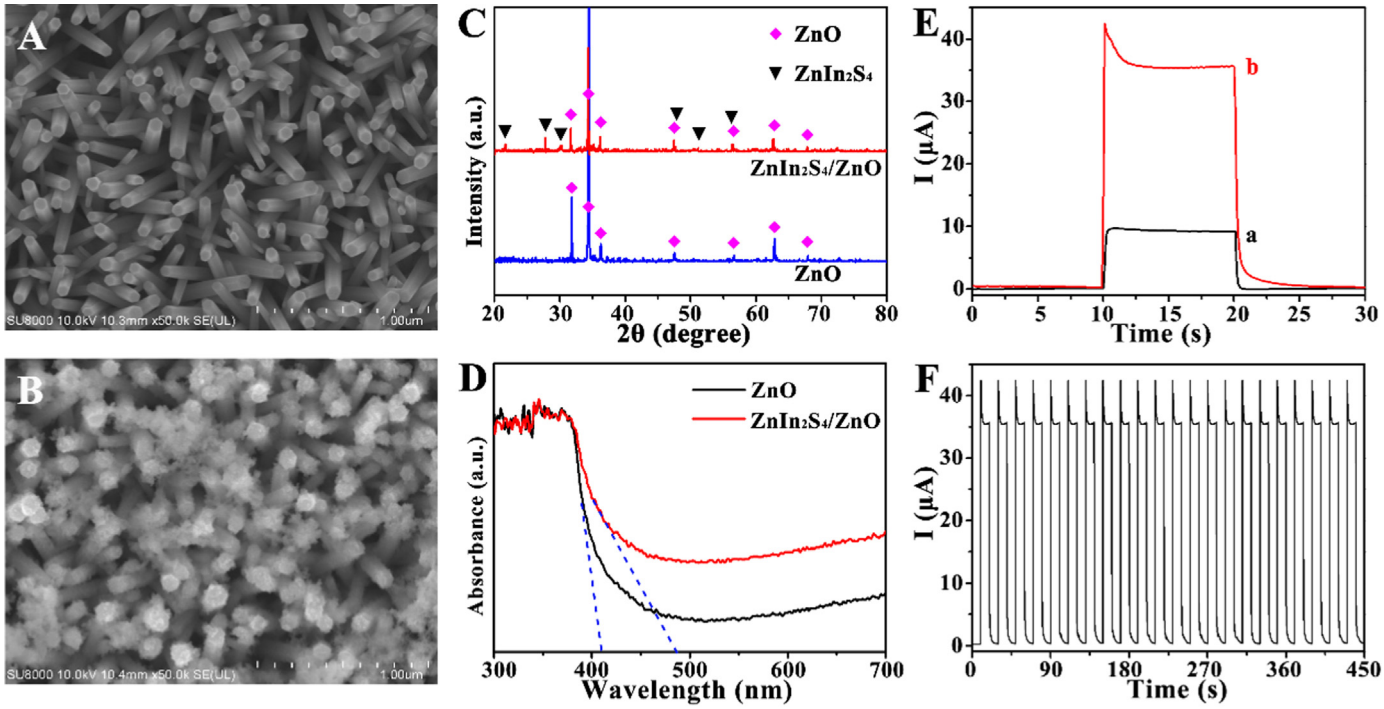

Fig. 1. SEM images of the (A) ZnO-NRs/ITO and (B) $ZnIn_2S_4$/ZnO-NRs/ITO electrodes; (C) XRD patterns of the ZnO-NRs (blue) and $ZnIn_2S_4$/ZnO-NRs (red); (D) UV–vis diffuse reflectance spectra of the ZnO-NRs (black) and $ZnIn_2S_4$/ZnO-NRs (red). (E) Photocurrent outputs of (a) the ZnO-NRs/ITO and (b) $ZnIn_2S_4$/ZnO-NRs/ITO electrodes; (F) time-varying photocurrent output of the $ZnIn_2S_4$/ZnO-NRs/ITO electrode. (For interpretation of the references to color in this figure legend, the reader is referred to the web version of this article).

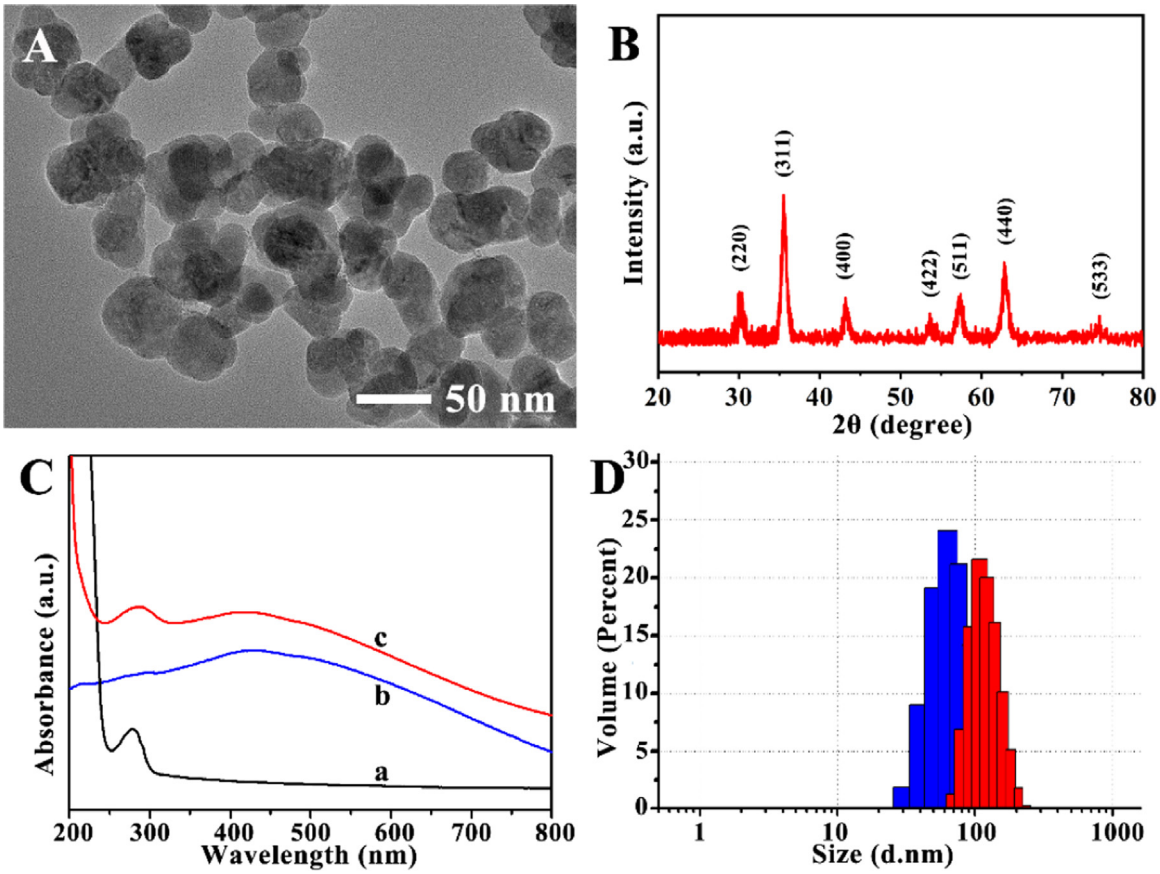

Fig. 2. (A) TEM image and (B) XRD pattern of the his-Fe_3O_4 nanoparticles; (C) UV–vis absorption spectra of (a) Ab_2, (b) his-Fe_3O_4, and (c) his-Fe_3O_4@Ab_2. (D) Hydrodynamic-size distribution of the his-Fe_3O_4 nanoparticles before (blue) and after (red) Ab_2 modification. (For interpretation of the references to color in this figure legend, the reader is referred to the web version of this article).

3.3. PEC properties of the $ZnIn_2S_4$/ZnO-NRs/ITO photoelectrode

As stated above, (i) coupling $ZnIn_2S_4$ with ZnO could evidently enhance the photocurrent output; (ii) both ZnO and $ZnIn_2S_4$ have good chemical stability. To verify the statement, photocurrent characterizations of the $ZnIn_2S_4$/ZnO-NRs/ITO photoelectrode were performed. As presented in Fig. 1E, at the optimum condition, the ZnO-NRs/ITO electrode exhibited a relatively small photocurrent output, because ZnO could harvest only the ultraviolet light (< 405 nm). After deposited $ZnIn_2S_4$ nanocrystals on the ZnO-NRs, the photocurrent output increased to 4 times higher than that of the ZnO-NRs/ITO electrode, which was because the ZnO-NRs/ITO electrode had a large specific surface area for plenty of $ZnIn_2S_4$ nanocrystals adhesion, and the deposited $ZnIn_2S_4$ extended the absorb range to visible light region. Fig. 1F presents time-varying photocurrent output of the $ZnIn_2S_4$/ZnO-NRs/ITO photoelectrode. It can be observed that the photocurrent output during each illumination segment nearly remain unchanged without obvious decay when the electrode suffered from repeated light irradiation, illustrating good stability of the $ZnIn_2S_4$/ZnO-NRs/ITO photoelectrode.

3.4. Characterizations of the his-Fe_3O_4 and his-Fe_3O_4@Ab_2 conjugate

Fig. 2A shows transmission electron microscopy (TEM) image of the synthesized his-Fe_3O_4 nanoparticles. It can be seen that the nanoparticles have smooth surfaces and an average diameter around of 30 nm. Fig. 2B displays typical XRD pattern of the his-Fe_3O_4 nanoparticles. All of the characteristic diffraction peaks at $2\theta = 30.2^\circ$, 35.6°, 43.2°, 57.4°, 62.7° and 74.1° could be assigned to (220), (311), (400), (511), (440), and (533) of spinel structure of Fe_3O_4 (JCPDS card no. 19-0629). Fig. 2C reveals UV–vis absorption spectrum of the obtained his-Fe_3O_4 @Ab_2 conjugate. As could be seen in curve a, the pure Ab_2 had a sharp characteristic absorption peak at 280 nm, which was derived from π–π* transition in the tyrosine and tryptophan residues of the proteins (Stoscheck, 1990). As shown in curve b, the his-Fe_3O_4 had a wide absorption range without any evident absorption peak in the wavelength scope. After Ab_2 was conjugated with his-Fe_3O_4, an absorption peak at 280 nm was clearly observed in curve c. The UV–vis spectra thus illustrated successful preparation of the his-Fe_3O_4@Ab_2 conjugates. Besides, the dynamic light scattering (DLS) was also used to perform the formation of the his-Fe_3O_4@Ab_2, as shown in Fig. 2D. The distribution of hydrodynamic size of the his-Fe_3O_4 nanoparticles after Ab_2 modification (red) become larger than that before Ab_2 modification (black), which further indicated successful conjugation between his-Fe_3O_4 and Ab_2.

3.5. Peroxidase-activity analysis of the his-Fe_3O_4 nanozyme

To verify high activity of the synthesized his-Fe_3O_4 nanozyme, peroxidase activities and catalytic parameters from Michaelis–Menten kinetic assays of the his-Fe_3O_4 and HRP were compared (Zhang et al., 2017; Fan et al., 2017b). Fig. 3A shows time-course of the UV–vis absorption curves of colorimetric reaction, and it can be clearly observed that the his-Fe_3O_4 nanozyme exhibited an evidently higher reaction rate than HRP as well as the blank. Further, utilizing the Michaelis-Menten model, the steady-state kinetic assay of H_2O_2 with the TMB and enzyme concentration fixation was determined, as shown in Fig. 3B. And the corresponding kinetic parameters were listed in Table 1. The K_M value of his-Fe_3O_4 for H_2O_2 was close to HRP, indicating relatively high affinity of his-Fe_3O_4 with H_2O_2. The k_{cat}/K_M value mirrors the catalytic efficiency of an enzyme for a given substrate. Notably, the k_{cat}/K_M value of the his-Fe_3O_4 for H_2O_2 was much higher than that of HRP, and this may ascribe to the fact that his-Fe_3O_4 surface has a lot of ferric and ferrous irons, each of which acts as the catalytic activity center of HRP (Wei and Wang, 2013; Zhou et al., 2017). Similarly, as shown in Fig. S2, the steady-state kinetic assay of TMB was investigated with the H_2O_2 and enzyme concentration fixation. And the related kinetic parameters were also listed in Table 1. The K_m value of his-Fe_3O_4 for TMB was obviously lower than HRP, illustrating high affinity between nanozymes and TMB (Gao et al., 2007; Wang et al., 2017). The same with H_2O_2 as the substrate, the k_{cat}/K_M value of the his-Fe_3O_4 for TMB was evidently higher than HRP, further confirming high activity of the synthesized his-Fe_3O_4 nanozyme.

3.6. Photocurrent characterization of the sensor development

The construction of the PEC immunoassay was monitored by photocurrent output, as shown in Fig. 3C. The $ZnIn_2S_4$/ZnO-NRs/ITO photoelectrode had a remarkable photocurrent output (curve a). After CS, Ab_1 and BSA were modified in order on the photoelectrode, the photocurrent output weakened gradually (curves b-d) owning to weaker electron-transfer of CS and evident steric hindrance of proteins, pointing successful fabrication of the immunosensor. After treating the as-fabricated immunosensor with target Ag and then his-Fe_3O_4@Ab_2 conjugate, the photocurrent decreased (curves e and f). Note that the photocurrent decrement toward target Ag anchoring was less than that of the subsequently anchored his-Fe_3O_4@Ab_2, which was mainly attributed to an evident increase in steric hindrance of the his-Fe_3O_4@Ab_2 conjugate. After the immunosensor was finally incubated with H_2O_2 coexisting with 4-CN, a further decrease in photocurrent output was found (curve g), indicating that the insulating catalytic precipitation was produced on the electrode. Thus, the photocurrent change demonstrated successful development of the PEC immunoassay. Besides, electrochemical impedance spectroscopy (EIS) characterization of the sensor development was also performed (see Fig. S3), which further suggested its successful fabrication.

3.7. Optimal conditions of the sensor

To achieve a higher sensitivity of the PEC immunoassay, some important parameters were optimized. Fig. S4-A shows photocurrent response of the $ZnIn_2S_4$/ZnO-NRs/ITO photoelectrode obtained with varied SILAR cycles of $ZnIn_2S_4$ nanocrystals. The photocurrent intensity increased with the addition of SILAR cycle, and it reached a maximum with four SILAR cycle of $ZnIn_2S_4$ deposition. However, excessive deposition of the $ZnIn_2S_4$ evidently increased the diffusion resistance for electron motion, leading to the decreased photocurrent intensity. Fig. S4-B exhibits the photocurrent response of the immunosensor incubated in target Ag solution with extension of the incubation time. The photocurrent intensity decreased gradually along with the specific immunoreaction between Ab_1 and Ag happened, and it already came to a plateau at about 60 min afterward. Thus, 60 min was selected as the incubation time of target Ag. Fig. S4-C displays photocurrent signal of the immunosensor undergoing catalytic precipitation with different times. It could be observed that photocurrent signal rapidly declined with the starting of catalytic precipitation, and then nearly tended to be a constant at about 10 min. Hence, 10 min of catalytic precipitation was selected.

3.8. Analytical performances

The PEC detection of target Ag was based on change degree of the photocurrent signal issuing from the specific sandwich immunoreactions between Ab_1 and target Ag as well as target Ag and his-Fe_3O_4@Ab_2 conjugate. As displayed in Fig. 3D, within the wide range of the concentration from 50 fg/mL to 1 ng/mL, the photocurrent signal weakened linearly with the increase of logarithm of target Ag concentration. The regression equation was $I = 15.93 - 3.18 \log C_{PSA}$ (pg/mL), with a correlation coefficient of 0.9988. The limit of detection (LOD, S/N = 3) for target Ag concentration was calculated to be 18 fg/mL (The calculation procedure for the LOD was presented in the Supporting information). For analytical performance comparison, most

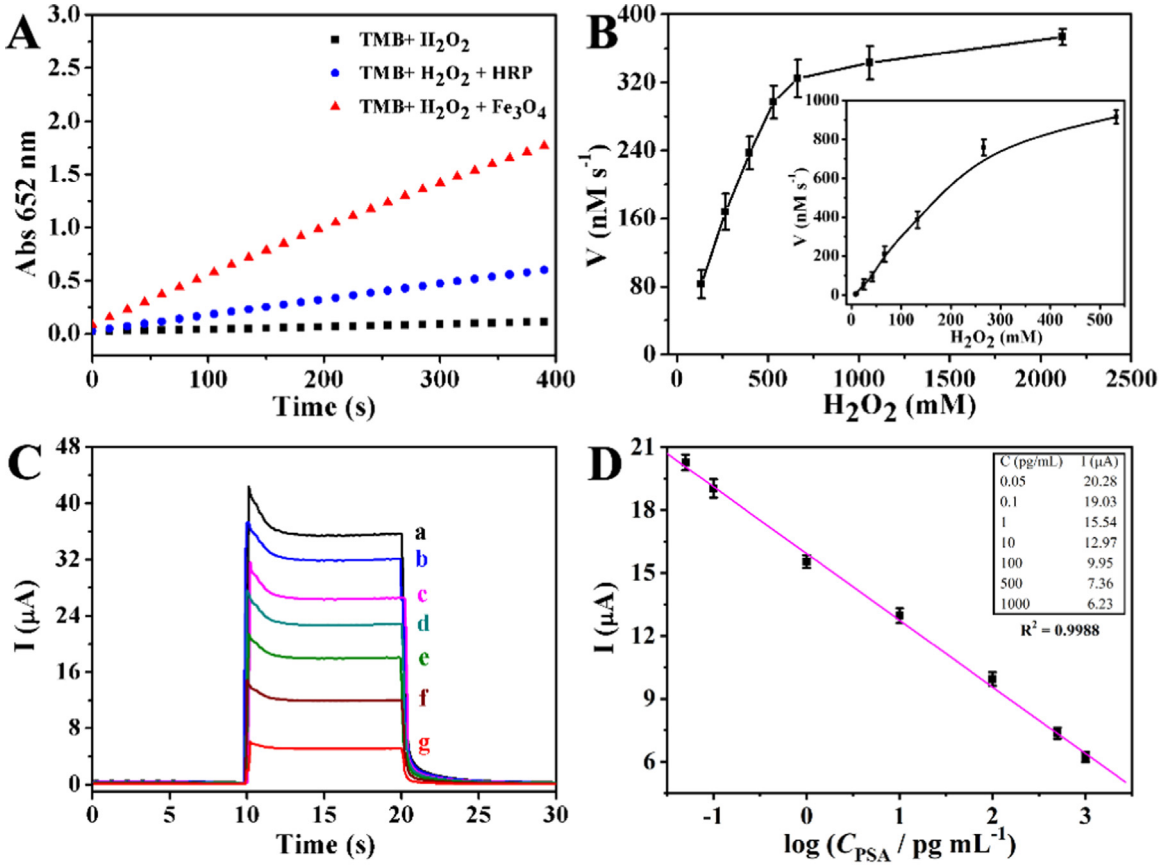

Fig. 3. (A) Time-course of the UV–vis absorption of colorimetric reaction monitored at 652 nm with his-Fe_3O_4, HRP, or the blank. (B) Steady-state kinetic assay of H_2O_2 catalyzed by his-Fe_3O_4 or HRP. (C) Photocurrent outputs of (a) the $ZnIn_2S_4$/ZnO/ITO photoelectrode, (b) after CS coating, (c) after Ab_1 immobilization, (d) after BSA blocking, (e) after incubation with Ag, (f) after further incubation with his-Fe_3O_4@Ab_2, and (g) after finally incubation with H_2O_2 and 4-CN. (D) Calibration curve of the proposed PEC immunoassay toward the detection of different concentrations of target Ag.

Table 1
Comparison of the kinetic parameters of his-Fe_3O_4 and HRP.

Catalyst	Substrate	[E] (M)	K_M (mM)	V_{max} (nM s^{-1})	k_{cat} (10^5 s^{-1})	k_{cat}/K_M (10^6 s^{-1} M^{-1})
His-Fe_3O_4	H_2O_2	8.6×10^{-13}	10.58	145.9	1.6965	16.04
HRP	H_2O_2	2.7×10^{-11}	9.15	63.8	0.0236	0.26
His-Fe_3O_4	TMB	8.6×10^{-13}	6.22	157.0	1.8256	29.35
HRP	TMB	2.7×10^{-11}	89.15	669.1	0.2478	0.27

Notes: [E], K_M, and V_{max} represent the enzyme concentration, the Michaelis-Menten constant, and the maximal reaction velocity, respectively. k_{cat} was calculated via the formula of $k_{cat} = V_{max}/[E]$.

of the previous reported enzyme-labeling PEC immunoassays were gathered in Table S1. And the comparing results convinced that the elaborated PEC immunoassay owned a superior or comparable LOD due to combined effects of superior signal amplification of the high-activity his-Fe_3O_4 nanozyme and excellent PEC properties of the $ZnIn_2S_4$/ZnO/ITO photoelectrode. In addition, specificity, repeatability and stability of the PEC immunoassay were also evaluated (see the Supporting information), and satisfactory results were acquired. The feasibility of the developed PEC immunoassay was investigated preliminarily through the recovery experiment in human serum samples. From the results listed in Table S2, it could be acquired that the recoveries of three samples for the added PSA with 1, 20, and 100 pg/mL were 95.8%, 106.1%, and 98.2%, respectively, which indicated a potential practical application in biological samples of this PEC immunoassay.

4. Conclusion

In summary, high-activity nanozyme instead of natural enzyme as signal amplifier was first introduced in PEC immunoassay for ultrasensitive detection of target biomarker. As signal amplifier, the his-Fe_3O_4 nanozyme exhibited obviously higher catalytic activity than natural enzyme HRP, and it also had the characteristics of simple preparation, low cost of production, and easy modification. The $ZnIn_2S_4$/ZnO-NRs/ITO photoelectrode as low-toxic PEC matrix had excellent properties of evident photocurrent output and good stability. Benefiting from combined effects of high activity of the his-Fe_3O_4 nanozyme and excellent PEC properties of the $ZnIn_2S_4$/ZnO-NRs/ITO photoelectrode, the pleased sensitivity of this PEC immunoassay was realized. Although the activities of the most other nanozymes need further improvement, they are ideal alternatives for corresponding natural enzyme toward the labeling PEC immunoassay in the near future.

Acknowledgments

This work is supported by the National Natural Science Foundation of China (21603099 and 21675093), the Taishan Scholar Project of Shandong Province (ts20110829), and State Key Laboratory of Analytical Chemistry for Life Science (SKLACLS1802).

Appendix A. Supporting information

Supplementary data associated with this article can be found in the online version at https://doi.org/10.1016/j.bios.2018.11.043.

References

Asati, A., Santra, S., Kaittanis, C., Nath, S., Perez, J.M., 2009. Angew. Chem. Int. Ed. 48, 2308–2312.
Bai, Z.M., Yan, X.Q., Kang, Z., Hu, Y.Q., Zhang, X.H., Zhang, Y., 2015. Nano Energy 14, 392–400.
Cao, J.T., Wang, B., Dong, Y.X., Wang, Q., Ren, S.W., Liu, Y.M., Zhao, W.W., 2018. ACS Sens. 3, 1087–1092.
Dong, Y.X., Cao, J.T., Wang, B., Ma, S.H., Liu, Y.M., 2018. ACS Appl. Mater. Interfaces 10, 3723–3731.
Fan, G.C., Han, L., Zhang, J.R., Zhu, J.J., 2014. Anal. Chem. 86, 12398–12405.
Fan, G.C., Zhu, H., Du, D., Zhang, J.R., Zhu, J.J., Lin, Y.H., 2016. Anal. Chem. 88, 3392–3399.
Fan, D.W., Ren, X., Wang, H.Y., Wu, D., Zhao, D., Chen, Y.C., Wei, Q., Du, B., 2017a. Biosens. Bioelectron. 87, 593–599.
Fan, K., Wang, H., Xi, J., Liu, Q., Meng, X., Duan, D., Gao, L., Yan, X., 2017b. Chem. Commun. 53, 424–427.
Gao, L., Zhuang, J., Nie, L., Zhang, J., Zhang, Y., Gu, N., Wang, T., Feng, J., Yang, D., Perrett, S., Yan, X., 2007. Nat. Nanotechnol. 2, 577–583.
Gao, L.Z., Fan, K.L., Yan, X.Y., 2017. Theranostics 7, 3207–3227.
Ge, S.G., Liang, L.L., Lan, F.F., Zhang, Y., Wang, Y.H., Yan, M., Yu, J.H., 2016. Sens. Actuators, B 234, 324–331.
Greene, L.E., Law, M., Goldberger, J., Kim, F., Johnson, J.C., Zhang, Y., Saykally, R.J., Yang, P., 2003. Angew. Chem. Int. Ed. 42, 3031–3034.
Haddour, N., Chauvin, J., Gondran, C., Cosnier, S., 2006. J. Am. Chem. Soc. 128, 9693–9698.
Han, J.H., Liu, Z.F., Guo, K.Y., Wang, B., Zhang, X.Q., Hong, T.T., 2015. Appl. Catal. B 163, 179–188.
Li, Y.J., Ma, M.J., Zhu, J.J., 2012. Anal. Chem. 84, 10492–10499.
Liang, M.M., Liu, S.L., Wei, M.Y., Guo, L.H., 2006. Anal. Chem. 78, 621–623.
Lin, Y.X., Zhou, Q., Tang, D.P., Niessner, R., Yang, H.H., Knopp, D., 2016. Anal. Chem. 88, 7858–7866.
Liu, Q., Lu, Hao, Shi, Z.W., Wu, F.L., Guo, J., Deng, K.M., Li, L., 2014. ACS Appl. Mater. Interfaces 6, 17200–17207.
Ludwig, J.A., Weinstein, J.N., 2005. Nat. Rev. Cancer 5, 845–856.
Mu, J.S., Zhang, L., Zhao, M., Wang, Y., 2014. ACS Appl. Mater. Interfaces 6, 7090–7098.
Mu, J.S., Zhao, X., Li, J., Yang, E.C., Zhao, X.J., 2016. J. Mater. Chem. B 4, 5217–5221.
Sahab, Z.J., Semaan, S.M., Sang, Q.X., 2007. Biomark. Insights 2, 21–43.
Shu, J., Qiu, Z.L., Zhou, Q., Lin, Y.X., Lu, M.H., Tang, D.P., 2016. Anal. Chem. 88, 2958–2966.
Singh, N., Savanur, M.A., Srivastava, S., D'Silva, P., Mugesh, G., 2017. Angew. Chem. Int. Ed. 56, 14267–14271.
Stoscheck, C.M., 1990. Methods Enzymol. 182, 50–68.
Tian, L., Qi, J., Oderinde, O., Yao, C., Song, W., Wang, Y., 2018. Biosens. Bioelectron. 110, 110–117.
Veitch, N.C., 2004. Phytochemistry 65, 249–259.
Wang, G.L., Shu, J.X., Dong, Y.M., Wu, X.M., Li, Z.J., 2015. Biosens. Bioelectron. 66, 283–289.
Wang, G.L., Xu, J.J., Chen, H.Y., Fu, S.Z., 2009a. Biosens. Bioelectron. 25, 791–796.
Wang, G.L., Yu, P.P., Xu, J.J., Chen, H.Y., 2009b. J. Phys. Chem. C 113, 11142–11148.
Wang, G.M., Yang, X.Y., Qian, F., Zhang, J.Z., Li, Y., 2010. Nano Lett. 10, 1088–1092.
Wang, K., Chen, J.J., Zhou, W.L., Zhang, Y., Yan, Y.F., Pern, J., Mascarenhas, A., 2008. Adv. Mater. 20, 3248–3253.
Wang, Q.Q., Zhang, X.P., Huang, L., Zhang, Z.Q., Dong, S.J., 2017. ACS Appl. Mater. Interfaces 9, 7456–7471.
Wang, X.Y., Cao, W., Lin, T.S., Chen, W., Lin, S.C., Yao, J., Zhao, X.Z., Zhou, M., Hang, C., Wei, H., 2017. Theranostics 7, 2277–2286.
Wei, H., Wang, E.K., 2008. Anal. Chem. 80, 2250–2254.
Wei, H., Wang, E.K., 2013. Chem. Soc. Rev. 42, 6060–6093.
Weston, A.D., Hood, L., 2004. J. Proteome Res. 3, 179–196.
Wu, J., Li, S., Wei, H., 2018a. Nanoscale Horiz. 3, 367–382.
Wu, R., Fan, G.C., Jiang, L.P., Zhu, J.J., 2018b. ACS Appl. Mater. Interfaces 10, 4429–4438.
Yu, Y.X., Ouyang, W.X., Liao, Z.T., Du, B.B., Zhang, W.D., 2014. ACS Appl. Mater. Interfaces 6, 8467–8474.
Zhan, W.W., Kuang, Q., Zhou, J.Z., Kong, X.J., Xie, Z.X., Zheng, L.S., 2013. J. Am. Chem. Soc. 135, 1926–1933.
Zhang, Z., Choi, M., Baek, M., Deng, Z., Yong, K., 2016. Nano Energy 21, 185–197.
Zhang, Z., Zhang, X., Liu, B., Liu, J., 2017. J. Am. Chem. Soc. 139, 5412–5419.
Zhao, W.W., Chen, R., Dai, P.P., Li, X.L., Xu, J.J., Chen, H.Y., 2014. Anal. Chem. 86, 11513–11516.
Zhao, W.W., Ma, Z.Y., Yan, D.Y., Xu, J.J., Chen, H.Y., 2012a. Anal. Chem. 84, 10518–10521.
Zhao, W.W., Ma, Z.Y., Yu, P.P., Dong, X.Y., Xu, J.J., Chen, H.Y., 2012b. Anal. Chem. 84, 917–923.
Zhao, W.W., Xu, J.J., Chen, H.Y., 2018. Anal. Chem. 90, 615–627.
Zhou, Y.B., Liu, B.W., Yang, R.H., Liu, J.W., 2017. Bioconjugate Chem. 28, 2903–2909.